Journal of The Electrochemical Society, **161** (9) H431-H437 (2014)
0013-4651/2014/161(9)/H431/7/$31.00 © The Electrochemical Society

TiO_2–WO_3 Composite Nanotubes from Co–Sputtered Thin Films on Si Substrate for Enhanced Photoelectrochemical Water Splitting

Karumbaiah N. Chappanda,[a] York R. Smith,[b,*] Loren W. Rieth,[c] Prashant Tathireddy,[c] Mano Misra,[a,d] and Swomitra K. Mohanty[d,,z]**

[a]*Department of Electrical and Electronics Engineering, Birla Institute of Technology and Science, Pilani, Rajasthan 333031, India*
[b]*Metallurgical Engineering Department, University of Utah, Salt Lake City, Utah 84112, USA*
[c]*Electrical and Computer Engineering Department, University of Utah, Salt Lake City, Utah 84112, USA*
[d]*Chemical Engineering Department, University of Utah, Salt Lake City, Utah 84112, USA*

Electrochemical anodization of a Ti–W nano-composite thin films deposited on a Si substrate by simultaneous magnetron sputtering of Ti and W resulted in the formation of TiO_2–WO_3 nanotubular arrays. A change in the morphology of TiO_2–WO_3 composite nanotubes with varying percentage of W in Ti–W composite thin films was observed. With a W density of less than or equal to 1.75×10^{19} W atoms per cm^3 (after anodization), the morphology of the composite nanotubes were similar to that of plain TiO_2 nanotubes. Whereas with further increase in W density resulted in a nanoporous morphology. Ti–W composite films were also deposited on Si substrates with a 100 nm thick layer of tin doped indium oxide (ITO) to examine the PEC activity of the formed oxide composites. The TiO_2–WO_3 composite nanotubes with 1.05×10^{19} W atoms per cm^3 (3.15×10^{18} W atoms per cm^3 before anodization) demonstrated to be an optimal W density for this system, giving rise to 40% increase in photocurrent at 0.5 V (vs. Ag/AgCl) compared to plain TiO_2 nanotubes.

Manuscript submitted February 18, 2014; revised manuscript received May 7, 2014. Published May 21, 2014. This was Paper 1825 from the San Francisco, California, Meeting of the Society, October 27–November 1, 2013.

With the diminishing fossil fuel reserves,[1] research on generating alternative renewable fuels such as hydrogen[2,3] and biodiesel[4,5] has gained considerable interest. Much of the research effort has been focused on the production of hydrogen using cleaner methods such as photoelectrochemical (PEC) water splitting[6–8] and photobiological water splitting.[9] PEC water splitting using TiO_2 was first reported by Fujihima and Honda in 1972.[10] Other various photo-active materials such as Fe_2O_3,[11] WO_3,[12] In_2O_3,[13] ZnO,[14] GaPN,[15] and GaAsPN[15] have also demonstrated successful application in solar assisted hydrogen generation. Arguably one of the most investigated materials for solar-based applications, TiO_2 has been widely studied because of its photocorrosion resistance, non-toxic nature, and environmental friendliness. More specifically, self-ordering TiO_2 nanotubular arrays (T-NT), synthesized via electrochemical anodization have been investigated for numerous photocatalytic and photoelectrochemical applications[16–19] due to its improved charge transport over nanoparticle films, for example.[20] In order to enhance the efficiency of T–NT based PEC cells, various approaches have been made to modify the electrical and optical properties such as doping with carbon,[21] niobium,[22] nitrogen,[23] sulfur,[24] and chromium,[25] for example, have shown to improve PEC and photocatalytic activity. Other approaches such as light assisted T–NT synthesis[26] and flame annealing of T–NT[27] have also shown to enhance photocurrent densities. Composite materials such as CdS–TiO_2,[28] TiO_2–WO_3,[29,30] and carbon nanotube/TiO_2[31] have also shown to improve PEC responses. With a particular focus on TiO_2–WO_3 nanotubes, various synthesis methods have been reported such as anodization of Ti–W alloy,[32] emulsion electrospinning, thermal evaporation, thermal annealing,[33] sol–gel synthesis,[34] electrochemical deposition of WO_3,[30] anodization of Ti containing tungstate species.[35] However, TiO_2–WO_3 nanotubes synthesized from anodization of Ti–W thin films formed by co-sputtering deposition has not been widely investigated.

In this paper, we report the synthesis of TiO_2–WO_3 composite nanotubes (TW–NT) from thin films on Si substrates for improving PEC activity. The method adopted is economical and robust, allowing for the synthesis of a variety of valve metal oxide composite nanostructures. This technique has added advantages of having a stable/planar substrate, enabling the potential incorporation of the composite nanotubes into integrated circuits using microfabrication techniques. Moreover, when using metal foils, a significant percentage of the metal is used as the substrate/electrode and is underutilized, resulting in a waste of material. Thin film deposition techniques offer the advantage of controlling the thickness of the Ti film deposition and limiting wastage of materials.

Experimental

Thin film deposition.— Clean n-type (100) Si wafers with resistivity of 1–5 Ωcm and RMS roughness of less than 1 nm were used as substrates for synthesis of the composite nanotubes. Si wafer was chosen as the substrate since it is the most commonly used substrate in the semiconductor industry and is preferred as a substrate for processes such a thin film deposition. The wafers were subjected to wet thermal oxidation at 1000 °C to form ∼100 nm thick layer of silicon dioxide. The SiO_2 was grown to electrically isolate the TiO_2–WO_3 nanotube from the substrate. Figure 1 shows a schematic of the experimental used for depositing Ti–W composite films (Denton Discovery 18 sputtering system). The sputter chamber was pumped down to pressures < 2 μTorr before flowing Ar process gas required for sputtering. D.C. magnetron sputtering was used to deposit Ti, while W was simultaneously deposited via R.F. magnetron sputtering to form a composite Ti–W film. R.F. sputtering system was utilized for depositing W since the sputter rate is slower compared to D.C. sputtering system, providing better control for low percentage addition of W. Ti and W targets of 99.2–99.7% purity were purchased from Kurt. J. Lesker Co. Ltd. and used for sputtering. The sputtering was carried out at 2.5 mTorr Ar pressure. Ti was sputtered at 200 W while W was sputtered from 15–100 W to vary the Ti–W percentage composition. It should be noted that the W percentage was varied in separate runs. The sputtering power for W was held constant for the entire co-sputtering run deposition and the changed/increased for the next co-sputtering run. Below 15 W, the plasma would not ignite to sputter W. A 100 nm ITO layer was deposited (100 W D.C. power, 2.5 mTorr Ar pressure) as electrodes before depositing Ti–W film in the case of thin films used for PEC water splitting studies. For comparison of the PEC activity, plain Ti thin films (200 W D.C. power, 2.5 mTorr Ar pressure) with no W were also deposited onto ITO/Si. After sputtering, the wafer was cooled down to ambient temperature in vacuum to minimize the oxidation of sputtered Ti–W film.

Nanotube synthesis.— The Ti and Ti–W thin films were subjected to electrochemical anodization at ambient temperature using an

*Electrochemical Society Student Member.
**Electrochemical Society Active Member.
zE-mail: s.k.mohanty@utah.edu

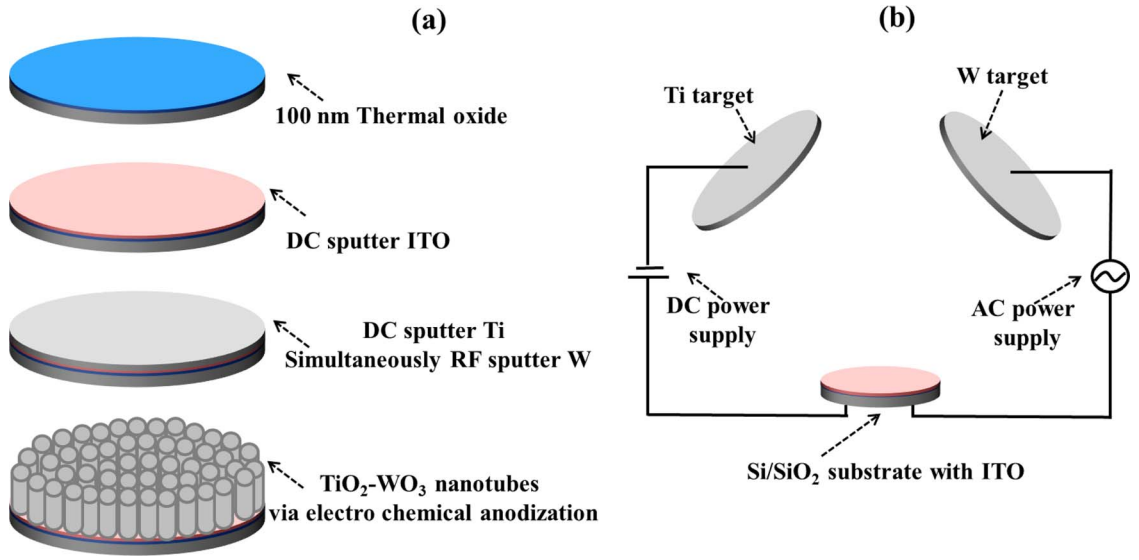

Figure 1. Schematic showing the experimental set up used for depositing W-Ti film and synthesis of TiO_2-WO_3 composite nanotube. (a) Shows the process step used for synthesis of TiO_2-WO_3 composite nanotube. (b) Shows the experimental set up used for deposition of Ti-W composite thin film achieved by simultaneously sputtering of Ti (using D.C. magnetron sputtering system) and W (using R.F. magnetron sputtering system).

organic electrolyte to form T–NT and TW–NT, respectively. The experimental set-up used was similar to our previous work.[36,37] In summary, Si wafers with Ti–W or Ti film were diced into 1 cm × 2 cm sized pieces. The organic electrolyte consisted of ethylene glycol (89.5 wt%, from Fisher Scientific), DI water (10 wt%), and ammonium fluoride (0.5 wt%, from Fisher Scientific).[38,39] The Ti films were cleaned with acetone and isopropanol alcohol followed by rinsing in DI water prior to anodization. Only approximately 1 cm^2 of the diced Ti–W/SiO_2/Si substrate was subjected to anodization under magnetic stirring of approximately 100 mL of electrolyte. The anodization voltage was ramped up at the rate of 1 V/s to 30 V (D.C.) and maintained until the film was completely anodized, marked by when the anodization current density dropped to zero on the power source (Agilent E3647A). The complete anodization time was approximately 20 minutes for plain Ti films, whereas 25 minutes for Ti-W films (i.e. W sputtered at 100 W). After anodization the samples were thoroughly rinsed in DI water. The samples were then dried in air and used for characterization studies. When preparing samples used for PEC testing, ammonium hydroxide solution (30 vol%) and hydrogen peroxide solution (30 vol%) at a ratio (volume) of 1:2 were used to etch a portion of Ti–W film in the diced samples, exposing the underlying ITO film which was then connected to positive terminal of the voltage source before anodization. The anodized films prepared at 20 V (D.C.) and were where subject to PEC testing. The anodized films used for PEC were subjected to calcination in stagnant air from 250–550°C for 2 hours with the temperature ramp up rate of 1.15°C/min.

Characterization and testing.— Scanning electron microscopy (SEM) micrographs from an FEI NanoNova SEM were used to study the change in the structural morphology of the anodized thin film with change in W percentage. All the top view micrographs were obtained at 200,000× magnification, and the side view micrographs were obtained at 250,000× magnification and 60° tilt. X-ray diffraction was used for identification and determination of the crystalline phases of the nanotubes using a Rigaku Miniflex XRD system. X-ray diffraction incidence angle was ranged from $2\theta = 20°–80°$ with 30 minutes irradiation time. Diffuse-reflectance UV–vis spectroscopy was used to characterize the bandgap of the T–NT and TW–NT using a Shimadzu UV-3600 UV-Vis-NIR spectrophotometer. An Agilent 7500ce inductively coupled plasma mass spectrometer (ICP-MS) with quadrupole mass spectrometer and an octopole reaction system to preferentially remove polyatomic interferences was used to analyze the atomic ratio of the W and Ti before and after anodization. A 193 nm fluorine-neon laser ablation was used to generate the aerosol of the Ti–W films. The laser was scanned at 40 μm/s at 3 pulses/s to limit the volume interaction of the laser to about 500 nm in depth. The W and Ti atomic percentages were determined by comparing the counts per second with a standard sample (NIST 610 glass) with elements of known concentration. A Kratos Axis Ultra DLD X-ray photoelectron spectrometer (XPS) was used to analyze the oxidation state of Ti–W anodized film. The samples were subjected to Ar ion cleaning. The photoelectrochemical activity of the composite anodes were examined under 1.5 AM irradiation with a Newport Solar Simulator (300 Xe Mercury lamp) in 0.5 M Na_2SO_4 (pH ~6.8). The photocurrent was monitored using a PARSTAT 4000 potentiostat where the composite films served as the photoanode, a platinum mesh as the cathode, and Ag/AgCl as the reference electrode.

Results and Discussion

Synthesis of TiO_2–WO_3 composite nanotubes.— Figure 1 shows the schematic set up used for depositing Ti–W films. The W deposition ranged from 5.25×10^{18} to 2.1×10^{19} atoms per cm^3 of Ti–W composite films (before anodization). The atomic density was determined using ICP MS along with the following equation for calculating the atomic ratios.[40]

$$C_E^{sm} = ((i_E/i_{IS})^{sm}/(i_E/i_{IS})^{std})(C_E/C_{IS})^{std}\left(C_{IS}^{sm}\right) \quad [1]$$

where C is the concentration, E is the element, IS is the element used as an internal standard, i is the intensity (counts per second, cps), sm denotes the sample, and std denotes the standard (NIST 610 glass). The standard glass sample consisted of 443 ppm of Ti, 440 ppm of In, 122 ppm of W, and 69.9 atomic% SiO_2.

The sputtering parameters used for depositing the composite film and the atomic ratio before and after anodization are shown in Table I. Figure 2 shows the SEM micrographs of the top and side view of Ti–W films after anodization. From Figure 2a and 2b it can be observed the anodized film has a tubular morphology similar to T–NT synthesized from thin Ti film (Figure S2 (c)). Increasing the W loading up to 1.2×10^{19} W atoms per cm^3 (before anodization) in Ti–W film resulted in a semi-tubular morphology. With further increase in W loading, the morphology of the anodized film results in nano-porous type layer as observed by Figure 2e–2h. The transition of a nano-tubular morphology to a more nano-porous morphology with increase in W loading is

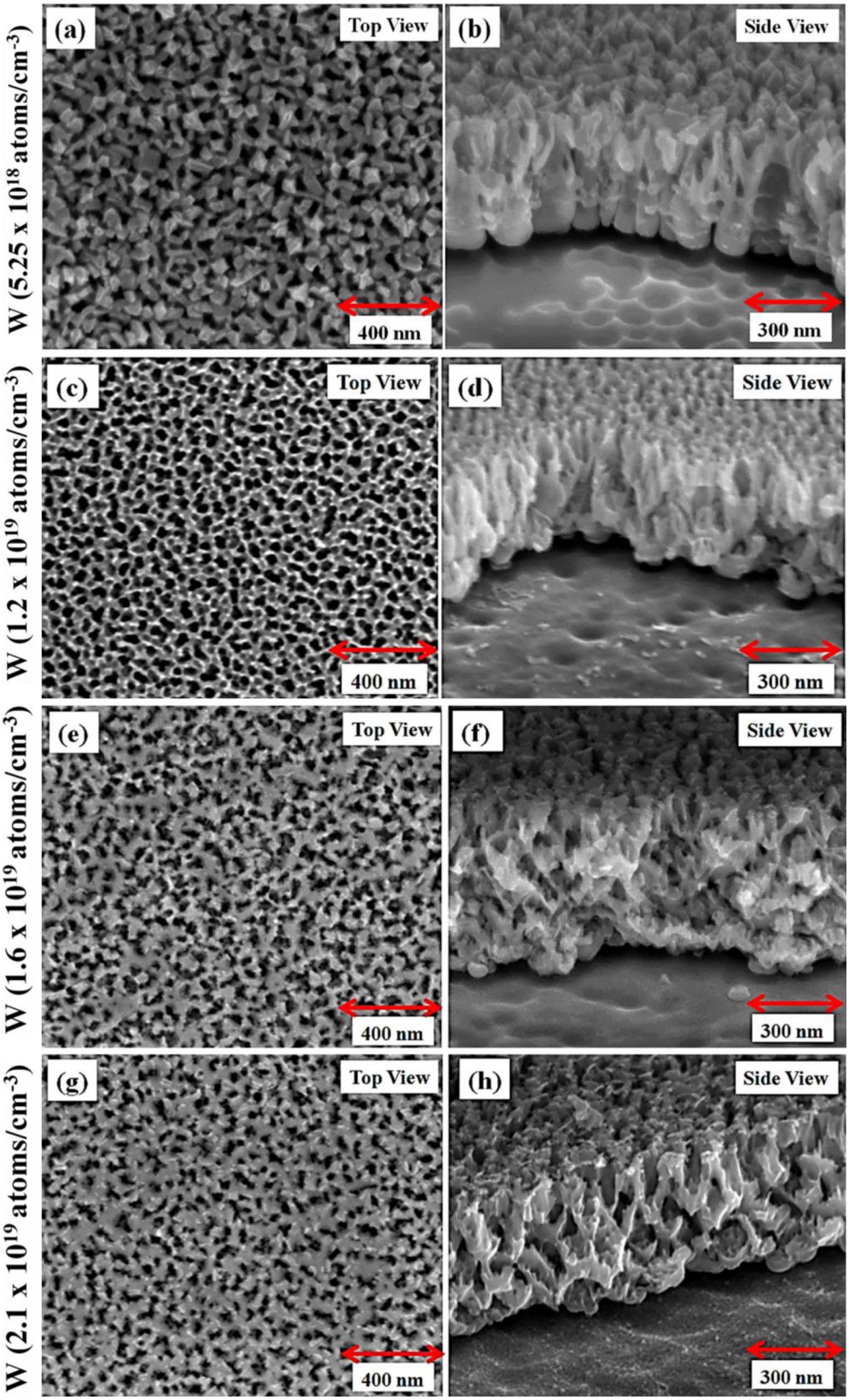

Figure 2. SEM micrographs showing the change is the morphology of anodized W-Ti film with the change is the W density. Figure 2 (a), (c), (e) and (g) shows the top view anodized film in which the W density is ranged from 5.25×10^{18} to 2.1×10^{19} atoms/cm^3 of Ti-W composite film (before anodization). Figure 2 (b), (d), (f) and (h) shows the side view of anodized film in which the W density is ranged from 5.25×10^{18} to 2.1×10^{19} atoms/cm^3 of Ti-W composite film (before anodization). With increase in W density, the morphology changes from tubular to nano-porous morphology

Table I. Shows the sputtering parameters used for depositing the Ti-W composite film and the Ti-W atomic ratio before and after anodization.

DC sputtering power (Watts)	Rf sputtering power (Watts)	Argon pressure (mTorr)	W (atoms/cm^3) Before anodization	W (atoms/cm^3) After anodization
200	25	2.5	5.25×10^{18}	1.75×10^{19}
200	50	2.5	1.2×10^{19}	4×10^{19}
200	75	2.5	1.6×10^{19}	5.34×10^{19}
200	100	2.5	2.1×10^{19}	7×10^{19}

due to the difference in the electrochemical etching rate of Ti and W. Fluoride ions in the electrolyte, etch W at a slower rate compared to Ti.[41,42] Due to this difference in etch rate there is more etching of Ti and hence more of W remains in the anodized film. With the increase in W percentage in the Ti–W composite film, the morphology of the nanotube is more influenced/pronounced by the unetched W. When the atomic percentage of tungsten is less than 5.25×10^{18} atoms per cm^3 (before anodization), the influence of the W is minimal on the morphology and takes on a nanotubular-type morphology as there is sufficient amount of Ti present to mask the non-tubularity caused by W in the anodized film. Also, various reports have shown that anodization of W, the resulting morphology is porous and not tubular WO_3.[43–45] The non-tubularity is attributed to the difference in stress from the formation of WO_3 and solubility of W by the electrolyte.[46] Moreover, the Pilling-Bedworth (P.B.) ratio of W to WO_3 (3.33) is higher than Ti to TiO_2 (1.73).[47] When the P.B. ratio is greater than 2, the oxide formed is not stable and often delaminates from the substrate due to induced surfaces stresses. Whereas when, $1 < P.B < 2$, the oxide formed is stable and self-passivates. Figure S1 shows the ICP-MS of Ti–W film before and after anodization (Ti-200 W, W-15 W sample) and is compared with a standard sample (NIST 610 glass) with known concentration of W, Ti and In. The counts/s of the Ti–W sample were compared with the standard sample along with their sensitivity factor to determine the atomic ratio. The Ti–W atomic ratio varied from 20,000:1 before anodization to 6,000:1 after anodization. The change in the Ti-W ratio before and after anodization is due to difference in the etch rates of Ti and W. Ti is etched at a faster rate retaining more of W atoms in the anodized films, thus a relative increase in W concentration compared to Ti is observed (Table I). It should be noted that there is also an increase in the volume of the films due to oxidation of the films. The change in the volume is not accounted for by using ICP-MS technique. Irrespective of the change in volume, the ICP-MS provides accurate technique for determining the Ti-W ratio. SEM micrographs of an anodized sample after laser ablation ICP-MS is shown in Figure S2 (a). During the ICP-MS measurements, the laser did not interact with the silicon dioxide substrate during generation of the aerosol and hence no Si was detected. From the change in the concentration ratio, it can be concluded that the electrolyte etches Ti at a relatively faster rate compared to W, hence is the observed non-tubular morphology with the increase in W atomic ratio. Figure S3 shows the XPS of a Ti–W film annealed at 350°C. Using the peak position of physisorbed carbon as the correction factor, the binding energy peak of Ti $2p_{1/2}$ and $2p_{3/2}$ was found to be at about 464.3 and 458.9 eV, suggesting that the Ti is predominately in Ti^{4+} oxidation state.[48] The oxidation state of tungsten could not be determined accurately because the 3p peak of Ti overlaps with the W 4f peak. Due to the low concentration of W, no other W peaks were visible in the XPS spectrum. However, there was a considerable amount of non-linearity observed in the Ti 3p and W 4f overlapped peak inferring the presence of trace amount of W. Figure S3 (b) shows the XPS spectrum showing the Ti 3p and W 4f overlapping peaks. Using CasaXPS software for peak fitting, the binding energy peaks of W $4f_{5/2}$ and $4f_{7/2}$ was found to be at approximately 37.3 and 35.3 eV, respectively, implying that the W is predominately in the W^{6+} oxidation state.[49] In addition, when W is calcinated under similar temperatures and environment as in this study, the oxidation state of W is reported to predominantly be W^{6+}.[50,51] Using the XPS fit, the atomic percentage of W was found to be 1.6 at%, which is significantly larger when compared to ICP-MS results. This discrepancy arises due to the elemental probing depth of XPS, which is about 1–10 nm (depending on the sample), only providing elemental surface composition. An important point to be noted is that the composite films were deposited using a two sputtering system. Controlling the sputtering time controlled the thickness of the film. The process of stopping the sputtering process is performed manually (using shutters controlled by switches) and there is a human error factor involved in accurately stopping both the sputtering process at the same time. This slight difference in stopping the sputtering process can have a significant difference in atomic percentages especially when probing depths ranging from 1–10 nm. As a result, XPS analysis was only used for determining the oxidation state of the metal oxides and does not necessarily represent the overall atomic composition of the oxide films. Hence ICP-MS was used to determine the Ti–W ratio, which has a larger depth probing capability. Also after anodization, the WO_3 percentages may be significantly different on the top portion of the nanotubes in comparison to the entire length of the nanotubes, since the top portion consists of nano-porous morphology, in comparison to the tubular structure of the remaining portion of the anodized films. From the top view SEM micrographs in Figure 2, the nanoporous layer can be observed, which is due to the influence of the native TiO_2 and WO_3 formed by exposure to the atmosphere as well as due to the presence of pronounced surface grains.[36,37] Therefore, the TiO_2–WO_3 ratio may also vary since the oxide formed is due to the exposure to the atmosphere and not via anodization. A significant influence on the morphology of the top nanoporous layer of the anodized films with an increase in W loading can also be observed.

Photoelectrochemical activity of TiO_2–WO_3 composite nanotube.— From experimental runs it was found that the optimum percentage of W is about 1.05×10^{19} atoms per cm^3 (3.15×10^{18} per cm^3 before anodization, SEM image of the TiW film before anodization is given in Figure S4.) for the highest photocurrent density. Figure 3 shows the change in the photocurrent density with WO_3 loading after anodization and annealing at 350°C. The TW–NT showed the maximum photocurrent density of 0.42 mA cm^{-2} at 0.5 V (vs. Ag/AgCl) for a W loading of 1.05×10^{19} atoms per cm^3 (3.15×10^{18} per cm^3 before anodization). The dark current (in the absence of light) irrespective of the W percentage was very minimal (less than 5 μA cm^{-2}) showing that the current density is mainly attributed to photo-induced charge carriers. In comparison with T–NT, the TW–NT demonstrates a 40% increase in the photocurrent density at 0.5 V (vs. Ag/AgCl). The increase in photocurrent density is due to the properties of WO_3. When WO_3 is in contact with TiO_2, the lifetime of the electron hole pair generated when the photoactive anode is reported to increase.[50]

During the morphology change with W loading studies, it was observed that the film would delaminate during anodization when the W loading is at or above 2.1×10^{19} atoms per cm^3 (concentration before anodization). The film would be further prone to delaminating when exposed to higher temperature during calcination. Beyond a certain W loading (3.15×10^{18} atoms per cm^3, before anodization), the photocurrent density is observed to reduce, which may be due to reduced electrical contact with ITO from the unstable film. Currently, there are no reports on high aspect ratio WO_3 nano-pores, as generally the oxide films delaminate from the substrate due to stress-induced mismatch of W/WO_3 surface,[46] which can also be corroborated from the high P.B. ratio. To understand the effect of the electrical contact of

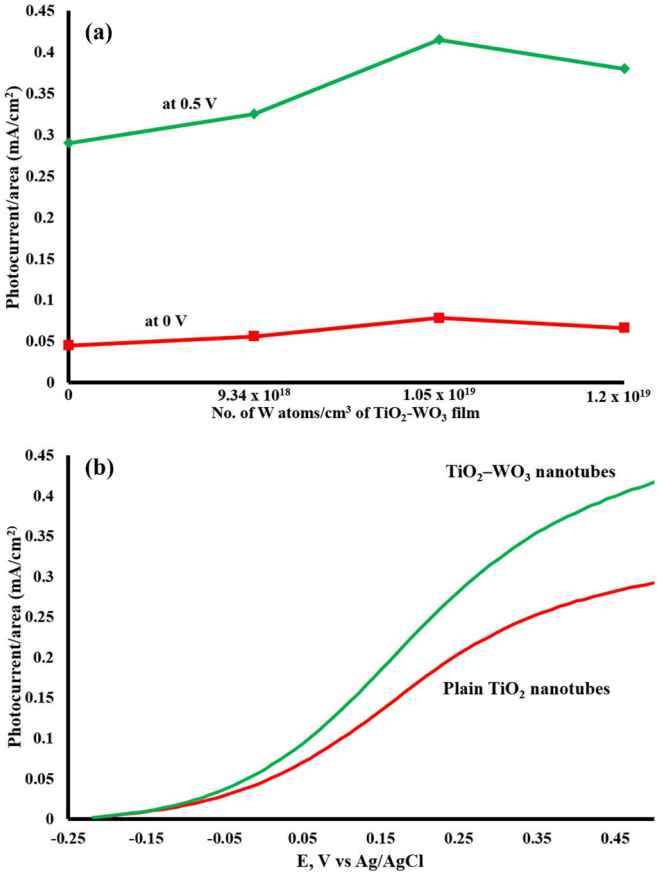

Figure 3. Shows the change in the photocurrent density of PEC cell with the change in the WO_3 density. The PEC shows 40% increase in the performance with 1.05×10^{19} W atoms per cm^3 (3.15×10^{18} per cm^3 before anodization) when compared to plain T-NT. The photocurrents were measured at 0.5 and 0 V. The calcinations temperature was 350°C. Figure 3 (b) shows the comparison of the photocurrents of composite and plain nanotubes.

the TW–NT to the ITO a study on the change in photocurrent density with nanotube length was carried out. Figure 4 shows the change in photocurrent density with length of the nanotube layer. Synthesis of composite nanotubes with low W loading such as 1.05×10^{19} per cm^3 (3.15×10^{18} per cm^3 before anodization) show synthesis behavior similar to plain T-NT as seen in our previous work.[36,37] Therefore

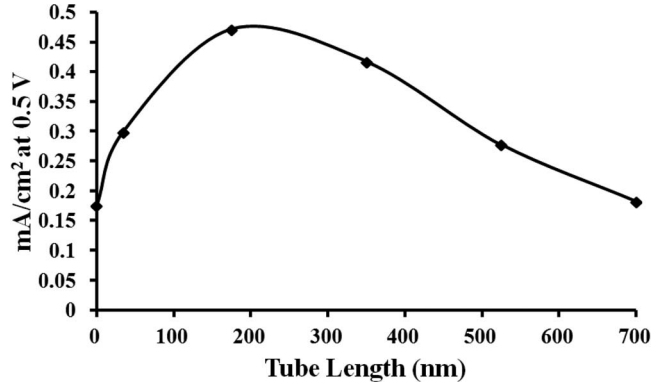

Figure 4. Shows the change in the photocurrent density of the PEC with the length of the composite nanotube. 500 nm thick Ti-W film on anodizing such that the length of the TW-NT is 200 nm shows the highest photocurrent density. The photocurrent was measured at 0.5 V and calcination temperature was 350°C. The nanotubes consisted of 1.05×10^{19} W atoms per cm^3 (3.15×10^{18} per cm^3 before anodization).

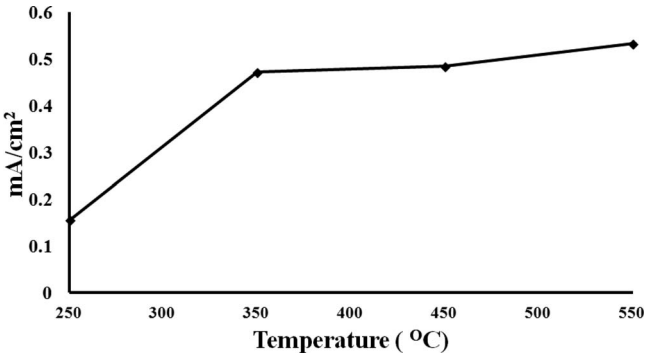

Figure 5. Shows the change is the photocurrent density of the PEC with annealing temperature. The photocurrent was measured at 0.5 V. The annealing time was 2 hours. The temperature was ramped at 1.15°C min^{-1}. The nanotubes consisted of 1.05×10^{19} W atoms per cm^3 (3.15×10^{18} per cm^3 before anodization). The length of the composite nanotubes were 200 nm.

the length of the nanotubes was varied by controlling the anodization time (0 to 20 min). The thickness of the Ti–W film used was 500 nm and the calcination temperature was 350°C. From Figure 4 it can be seen that photocurrent density was the highest when the length of the TW–NT was 200 nm. Upon completely anodizing the film, the nanotube length is 700 nm, which is 1.4 times longer than the thickness of the Ti–W deposited film which is due the oxidation of Ti and W during anodization.[36,37] With the increase in the length of the nanotube (above 200 nm), the nanotubes are less stable and do not make a good electrical contact with the ITO. With decrease in the nanotube length (less than 200 nm) the electrical contact is improved, however the photocurrent density reduces due to the decrease in the surface area to volume ratio. Therefore, there is a need for an optimal Ti–W thickness to be present for stable oxide layer to form with high PEC performance. The change in the photocurrent density and stability of the oxide layer with calcination temperature was also examined. Figure 5 shows the change in photocurrent density with annealing temperature. From the experiments so far, it was observed that 200 nm long TW-NT with 1.05×10^{19} W atoms per cm^3 (after anodization) had the highest photocurrent density. Therefore, TW-NT of the similar length and W loading were subject to different calcination temperature to optimize the calcination. The lowest photocurrent density was observed when samples were annealed at 250°C and increased upon an increase in annealing temperature. This is because at 250°C there is little crystallization that occurs and the nanotubes are still amorphous. This can was confirmed from the XRD results in Figure 6. When annealed at 350°C and 450°C, TiO_2 forms anatase phase predominantly and hence the photocurrent increases. When annealed at 550°C, TiO_2 is partly transferred to rutile phase[52] thereby improving the photocurrent. The

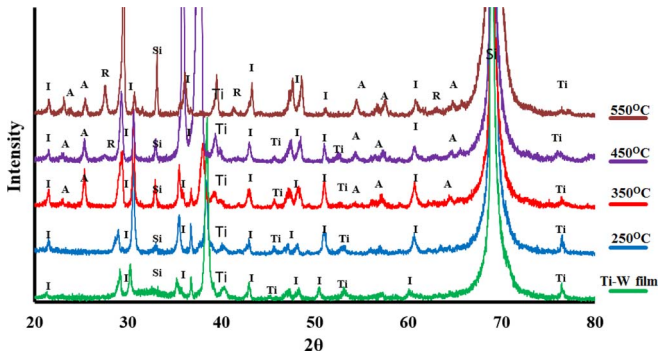

Figure 6. Shows the XRD of TW-NT samples annealed at 250°C to 550°C and unanodized Ti-W film. The 'I' implies ITO. 'A' implies anatase and 'R' implies rutile polymorphs of TiO_2. The nanotubes consisted of 1.05×10^{19} W atoms per cm^3 (3.15×10^{18} per cm^3 before anodization).

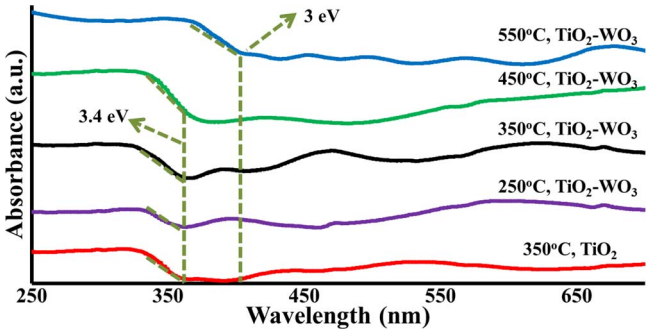

Figure 7. Shows diffuse reflectance UV-Vis spectrum of the TW-NT annealed at temperatures from 250 to 550°C and plain TiO_2 nanotubes annealed at 350°C. Up to 450°C, the bandgap of TW-NT was 3.4 eV. When annealed at 550°C the bandgap reduced to 3 eV due to formation of rutile TiO_2. The composite nanotubes consisted of 1.05×10^{19} W atoms per cm^3 (3.15×10^{18} per cm^3 before anodization).

XRD results do not show any presence of WO_3, which is due to the low atomic percentage. Figure 7 shows the diffuse reflectance UV-Vis spectroscopy of sample annealed from 250 to 550°C and as well as that of plain TiO_2 annealed at 350°C. For the samples annealed at 450°C and below, the bandgap is shown to be about 3.4 eV. However, when the sample is annealed at 550°C, the bandgap is reduced to 3 eV. The reduced bandgap is due to the formation rutile TiO_2[53] (Figure 6). The photocurrent density when annealed at 550°C is higher when compared to samples annealed at lower temperature due to formation of rutile titania. The change in the bandgap is not due to the presence of WO_3 as a significant amount of WO_3 or with doping/alloying of WO_3 with TiO_2, the bandgap would be less than 3 eV.[54] Therefore, the increase in the photocurrent density can be attributed not only to the hole affinity property of WO_3, but also the synergistic effect between anatase and rutile titania.[55] When annealed at temperatures above the 550°C the film delaminates decreasing the photocurrent density. The optimal samples were potentiostatically held at 0.5 V (vs. Ag/AgCl) for 1 h under illumination and the photocurrent density was observed to be stable. Top view SEM micrograph image of the composite nanotube after 1 h of irradiation is shown in Figure S2 (b). It was observed that there was no change in the morphology showing the stability of the nanotubes.

In brief, TW-NT synthesized from 500 nm thick co-sputtered Ti-W composite films with 3.15×10^{18} atoms/cm^3 W loading resulted in a 40% increase in photocurrent density compared to plain T-NT. TW-NT anodized films with 200 nm and annealed at 550°C resulted in a photocurrent density of 0.5 mA/cm^2 at 0.5 V. Enhanced photocurrent density using a TiO_2-WO_3 can be attributed to the charge transfer occurring at the interface of the two materials. The difference in affinity to gain or lose electrons helps reduce to recombination losses.[56] The formation of localized TiO_2-WO_3 heterojunctions or through the formation of W^{6+} surface states, which act as a hole mediator for charge transfer to the electrolyte, can also explain the observed enhanced photoelectrochemical performance in such systems.[57] For example, Smith et al. formed a TiO_2-WO_3 composite by adding phosphotungstic acid to the anodization electrolyte.[35] Improved photoelectrochemical performance was reported due to a reduction in charge transfer resistance at the semiconductor/electrolyte interface. Park et al. reported T-NT coated with WO_3 deposited via electrochemical deposition with photocurrents density of 2 mA/cm^2 at 1.2 V.[58] They attributed the enhanced photocurrent to the difference in electrochemical potential of the two phases formed by TiO_2-WO_3 composite thereby reducing recombination losses. The use of co-sputtering technique can achieve uniform distribution of WO_3 in the TiO_2 matrix and on the surface, which could potentially harness the advantage of reduced electron-hole recombination losses as per the above-mentioned mechanisms. Therefore use of simple low cost composite materials such as TiO_2 and WO_3 has a promising potential for water splitting application with increased photo conversion.

Conclusions

TiO_2–WO_3 composite nanotubes were successfully synthesized on a Si wafer by simultaneous sputtering of Ti and W to form Ti–W nanocomposite. Electrochemical anodization using an ethylene glycol organic electrolyte resulted in the formation of nanotubular and nanoporous TiO_2–WO_3 oxide layers. The change is morphology with change in W density in the Ti–W composite was studied and was observed that with less than 5.25×10^{18} W atoms per cm^3 (before anodization), the anodized film has a tubular morphology, while a further increase in W density, the anodized film changes from tubular morphology to a nano-porous morphology. Also with the increase in W density, the stability of the anodized film decreases, limiting the W loading capability in the oxide film. With 1.05×10^{19} W atoms per cm^3 in the anodized film, it is seen that the photocurrent density increased by 40% in comparison to plain T–NT. It was observed that there is a need for an optimal Ti–W thickness to be present for stable TW–NT to form, which would improve the photocurrent density compared to TW–NT photoanodes that are completely anodized. Studies with different annealing temperature showed that when annealed at 250°C, the nanotubes are amorphous resulting in low photocurrent density. When annealed at temperatures of 350°C and above, the anatase phase titania is formed, improving the charge transport properties and subsequent photocurrent density. When annealed at 550°C, partial rutile titania is formed and showing the highest photocurrent density of 0.52 mA cm^{-2} at 0.5 V (vs. Ag/AgCl). Scanning electron microscopy, X-ray diffraction, ICP-MS, X-ray photoelectron spectroscopy and diffuse reflectance UV-Vis spectroscopy were used to study the morphology, crystalline phases, atomic ratio, oxidation state and bandgap of the oxide films, respectively, to optimize the performance of the TW–NT in photoelectrochemical applications.

Acknowledgment

The work presented here was supported by the Utah Science and Technology Research (USTAR) initiative. The authors acknowledge Brain Baker and Steve Pritchett of the 'Utah Nanofab' at the University of Utah for the help with the Ti–W deposition, and Dr. Diego P. Fernandez for the running the ICP-MS experiments. YRS would also like to acknowledge support in the form of a Graduate Research Fellowship, University of Utah.

References

1. S. Shafiee and E. Topal, *Energy Policy*, **37**, 181 (2009).
2. C. Koroneos, A. Dompros, G. Roumbas, and N. Moussiopoulos, *Int. J. Hydrogen. Energ.*, **29**, 1443 (2004).
3. S. Crawford, E. Thimsen, and P. Biswasz, *J. Electrochem. Soc.*, **156**, H346 (2009).
4. N. Kondamudi, S. K. Mohapatra, and M. Misra, *J. Agric. Food Chem.*, **56**, 11757 (2008).
5. N. Kondamudi, J. Strull, M. Misra, and S. K. Mohapatra, *J. Agric. Food Chem.*, **57**, 6163 (2009).
6. S. U. M. Khan, M. Al-Shahry, and W. B. Ingler Jr., *Science*, **297**, 2243 (2002).
7. O. Khaselev and J. A. Turner, *J. Electrochem. Soc.*, **145**, 3335 (1998).
8. H. Wang and J. A. Turner, *J. Electrochem. Soc.*, **157**, F173 (2010).
9. E. Greenbaum, *Biophys. J.*, **54**, 365 (1988).
10. A. Fujishima and K. Honda, *Nature*, **238**, 37 (1972).
11. I. Cesar, A. Kay, J. A. G. Martinez, and M. Gratzel, *J. Am. Chem. Soc.*, **128**, 4582 (2006).
12. R. Abe, T. Takata, H. Sugiharaa, and K. Domen, *Chem. Commun.*, **128**, 3829 (2005).
13. K. R. Reyes-Gil, E. A. Reyes-Garcia, and D. Raftery, *J. Phys. Chem. C*, **111**, 14579 (2007).
14. X. Yang, A. Wolcott, G. Wang, A. Sobo, R. Fitzmorris, F. Qian, J. Z. Zhang, and Y. Li, *Nano Lett.*, **9**, 2331 (2009).
15. T. G. Deutsch, C. A. Koval, and J. A. Turner, *J. Phys. Chem. B*, **110**, 25297 (2006).
16. P. Acevedo-Peñaz and I. González, *J. Electrochem. Soc.*, **160**, H452 (2013).
17. M.-Y. Hsu, H.-L. Hsu, and J. Leu, *J. Electrochem. Soc.*, **159**, H722 (2012).
18. N. K. Allam, K. Shankar, and C. A. Grimes, *J. Mater. Chem.*, **18**, 2341 (2008).
19. K. Shankar, G. K. Mor, H. E. Prakasam, S. Yoriya, M. Paulose, O. K. Varghese, and C. A. Grimes, *Nanotechnology*, **18**, 065707 (2007).
20. A. Lamberti, A. Sacco, S. Bianco, D. Manfredi, F. Cappelluti, S. Hernandez, M. Quaglioa, and C. F. Pirri, *Phys. Chem. Chem. Phys.*, **15**, 2596 (2013).
21. J. H. Park, S. Kim, and A. J. Bard, *Nano Lett.*, **6**, 24 (2006).
22. C. Das, P. Roy, M. Yang, H. Jha, and P. Schmuki, *Nanoscale*, **3**, 3094 (2011).

23. O. Diwald, T. L. Thompson, T. Zubkov, Ed. G. Goralski, S. D. Walck, and J. T. Yates Jr., *J. Phys. Chem. B*, **108**, 6004 (2004).
24. X. Tang and D. Li, *J. Phys. Chem. C*, **112**, 5405 (2008).
25. H. Kato and A. Kudo, *J. Phys. Chem. B*, **106**, 5029 (2002).
26. Y. R. Smith, B. Sarma, S. K. Mohanty, and M. Misra, *ACS Appl. Mater. Interfaces*, **4**, 5883 (2012).
27. A. Mazare, I. Paramasivam, K. Lee, and P. Schmuki, *Electrochem. Commun.*, **13**, 1030 (2011).
28. Y. Yin, Z. Jin, and F. Hou, *Nanotechnology*, **18**, 495608 (2007).
29. W. Smith, A. Wolcott, R. C. Fitzmorris, J. Z. Zhang, and Y. Zhao, *J. Mater. Chem.*, **21**, 10792 (2011).
30. J. H. Park and O. O. Park, *Appl. Phys. Lett.*, **89**, 163106 (2006).
31. K. Dai, T. Peng, D. Ke, and B. Wei, *Nanotechnology*, **20**, 125603 (2009).
32. M. Li, G. Zhao, P. Li, Y. Zhang, and M. Wu, *Environ Technol.*, **33**, 191 (2012).
33. B. Lu, X. Li, T. Wang, E. Xie, and Z. Xu, *J. Mater. Chem. A*, **1**, 3900 (2013).
34. L. Cheng, X. Zhang, B. Liu, H. Wang, Y. Li, Y. Huang, and Z. Du, *Nanotechnology*, **16**, 1341 (2005).
35. Y. R. Smith, B. Sarma, S. K. Mohanty, and M. Misra, *Electrochem. Commun.*, **19**, 131 (2012).
36. K. N. Chappanda, Y. R. Smith, S. K. Mohanty, L. W. Rieth, P. Tathireddy, and M. Misra, *Nanoscale Res. Lett.*, **7**, 388 (2012).
37. K. N. Chappanda, Y. R. Smith, M. Misra, and S. K. Mohanty, *Nanotechnology*, **23**, 385601 (2012).
38. Y. R. Smith and V. Subramanain, *J. Phys. Chem. C*, **115**, 8376 (2011).
39. Y. S. Sohn, Y. R. Smith, V. R. Subramanian, and M. Misra, *Appl. Catal. B*, **84**, 372 (2008).
40. S. M. Eggins, *Geostandards Newsletter*, **27**, 147 (2007).
41. K. R. Williams, *J. Microelectromech. S.*, **5**, 256 (1996).
42. K. R. Williams, *J. Microelectromech. S.*, **12**, 761 (2003).
43. R. Hahn, J. M. Macak, and P. Schmuki, *Electrochem Commun*, **9**, 947 (2007).
44. H. Tsuchiya, J. M. Macak, I. Sieber, L. Taveira, A. Ghicov, K. Sirotna, and P. Schmuki, *Electrochem Commun*, **7**, 295 (2005).
45. N. R. de. Tacconi, C. R. Chenthamarakshan, G. Yogeeswaran, A. Watcharenwong, R. S. de Zoysa, N. A. Basit, and K. Rajeshwar, *J. Phys. Chem. B*, **110**, 25347 (2006).
46. P. Roy, S. Berger, and P. Schmuki, *Angew. Chem. Int. Ed.*, **50**, 2904 (2011).
47. N. B. Pilling and R. E. Bedworth, *J. Inst. Met.*, **29**, 529 (1923).
48. U. Diebold and T. E. Madey, *Surface Science Spectra*, **4**, 227 (1998).
49. R. Sivakumar, R. Gopalakrishnan, M. Jayachandran, and C. Sanjeeviraja, *Smart Mater. Struct.*, **15**, 877 (2006).
50. X. Yan, X. Zong, G. Q. Lu, and L. Wang, *Progress in Natural Science: Materials International*, **22**, 654 (2012).
51. J. R. Sohn, H. S. Cho, and H. W. Kim, *J. Ind. Eng. Chem.*, **5**, 1 (1999).
52. A. Tighineanu, T. Ruff, S. Albu, R. Hahn, and P. Schmuki, *Chem. Phys. Lett.*, **494**, 260 (2010).
53. S. Valencia, J. M. Marín, and G. Restrepo, *The Open Materials Science Journal*, **4**, 9 (2010).
54. C. Das, I. Paramasivam, N. Liu, and P. Schmuki, *Electrochimica Acta*, **56**, 10557 (2011).
55. Y. Luo, X. Liu, and J. Huang, *CrystEngComm*, **15**, 5586 (2013).
56. S. J. Wang, G. Cheng, X. H. Jiang, Y. C. Li, Y. B. Huang, and Z. L. Du, *Appl. Phys. Lett.*, **88**, 212108 (2006).
57. C. Das, I. Paramasivam, N. Liu, and P. Schmuki, *Electrochimica. Acta.*, **56**, 10557 (2011).
58. J. H. Park and O. O. Park, *Appl. Phys. Lett.*, **89**, 163106 (2006).